Supplementary Material for

Demonstration and Non-volatile Trimming of a Highly-Parallel, High-Capacity Silicon Micro-disk Transmitter

Chao Luan[1,*], Alex Sludds[1], Chao Li[1], Ian Christen[1], Ryan Hamerly[1,2], Dirk Englund[1]

[1] *Research Laboratory of Electronics, MIT, Cambridge, MA 02139, USA*
[2] *NTT Research Inc., PHI Laboratories, 940 Stewart Drive, Sunnyvale, CA 94085, USA*

I. VERTICAL P-N JUNCTION MICRODISK MODULATOR

Using the free-carrier dispersion effect, a variety of silicon-based resonant EOIMs have been demonstrated [18, 27, 29, 49–52]. The carrier-injection-based modulators offer significant amplitude modulation efficiency but are inherently limited in bandwidth due to the low mobility speed of the injected carriers [53–55]. The carrier accumulation modulators, employing metal-oxide-semiconductor (MOS) capacitors, provide efficient modulation and high bandwidth; however, they require complex fabrication processes involving additional thin oxide layers and poly-silicon depositions [56–58]. Conversely, carrier depletion resonant EOIMs operating under reverse-biased voltages achieve low energy consumption and high bandwidth but typically suffer from lower modulation efficiency. To address these limitations, vertical-type p–n junction microdisk EOIMs have been developed. The vertical junction configuration enables internal n^+ and p^+ electrical contacts, eliminating the necessity for a ridge waveguide structure and thus retaining a smooth, hard outer wall for the silicon microdisk resonator. This hard outer wall significantly enhances the optical mode confinement, allowing for the realization of extremely compact microdisk modulators with micrometer-scale diameters. Consequently, this design greatly reduces device capacitance, enabling large bandwidth and low energy consumption modulation. Additionally, the vertical junction microdisk modulators provide substantial spatial overlap between carriers and the optical mode, resulting in enhanced modulation efficiency [16–19, 27].

II. CHARACTERIZATION OF THE MICRO-DISK MODULATOR

A. Subsection 1: ER, IL, and OMA

Figure 6 summarizes the static optical-power metrics of the 64-channel microdisk transmitters when driven with a 2 V_{pp} electrical swing. For each wavelength we extract

- the IL: the on-resonance transmission of the '1' level relative to the input fiber power;
- the ER: ER $= P_1/P_0$ expressed in decibels, where P_1 and P_0 are the optical powers in the logical '1' and '0' states, respectively; and
- the OMA, defined in linear units as OMA $= P_1 - P_0$.

The devices exhibit a largest ER of 9.8 dB and an IL of 2.6 dB. The corresponding average OMA is -3.2 dB response to the input power in a 2-V voltage swing.

B. Extracting the waveguide absorption coefficient and refractive-index change

The through-port transmission of an all-pass micro-ring resonator is

$$T(\phi) = \frac{a^2 - 2ar\cos\phi + r^2}{1 - 2ar\cos\phi + (ar)^2}, \tag{1}$$

with $a = \exp(-\alpha L/2)$ and $L = 2\pi R$. Near an isolated resonance $\lambda = \lambda_0$ we expand $\phi \simeq \phi_0 + 2\pi L(\lambda - \lambda_0)/\big(\lambda_0^2/n_g\big)$; Eq. (1) then reduces to the Lorentzian form

$$T(\lambda) = 1 - \frac{A}{1 + \big[2(\lambda - \lambda_0)/\Delta\lambda\big]^2}, \tag{2}$$

whose three fit parameters provide the **loaded quality factor** $Q_L = \lambda_0/\Delta\lambda$ and the dip depth $T_{min} = 1 - A$.

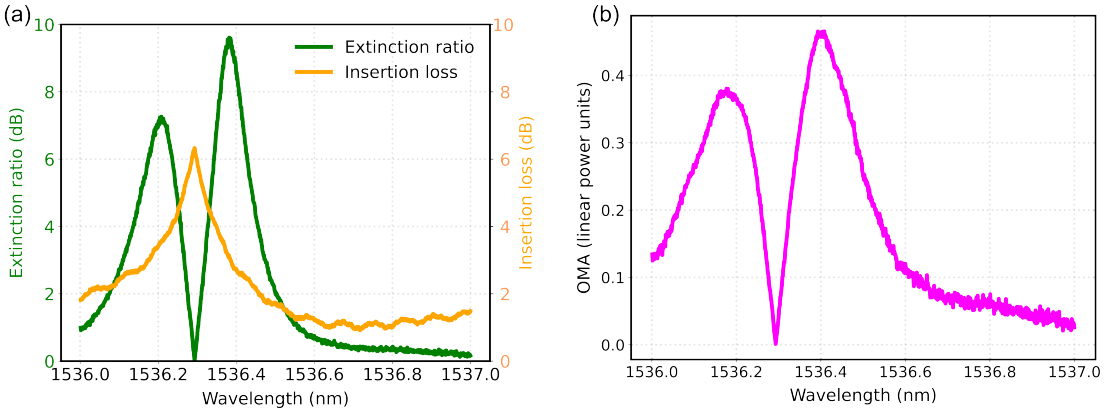

Figure 6. ER, IL and OMA results of the microdisk transmitter under a 2-V swing voltage.

a. Intrinsic Q: Following [59], the intrinsic quality factor is

$$Q_{\text{int}} = \frac{2\,Q_{\text{L}}}{1+\sqrt{T_{\text{min}}}}, \tag{3}$$

b. Propagation loss: The round-trip intrinsic loss then yields the linear wave-guide attenuation

$$\alpha = \frac{2\pi n_{\text{g}}}{Q_{\text{int}}\lambda_0}, \qquad \alpha_{\text{dB/cm}} = 4.343 \times 10^2\,\alpha \tag{4}$$

Applying Eqs. (1)–(4) to all the reverse-biased spectra and subtracting gives the bias-induced absorption change $\Delta\alpha = \alpha_{\text{biased}_1} - \alpha_{\text{biased}_2}$.

c. Effective–index change: The resonance condition for an m-th order mode is $m\lambda_0 = n_{\text{eff}}L$. Differentiating and holding L fixed gives $\Delta n_{\text{eff}}/n_{\text{eff}} = \Delta\lambda/\lambda_0$, so the bias-induced effective-index change is

$$\Delta n_{\text{eff}} = n_{\text{g}}\,\frac{\Delta\lambda}{\lambda_0} \tag{5}$$

where $\Delta\lambda = \lambda_{\text{biased1}} - \lambda_{\text{biased2}}$ is the measured wavelength shift and n_{g} is the group index obtained from the waveguide dispersion calculation. Combining Eqs. (4) and (5) therefore yields both the absorption and refractive-index changes of the micro-disk from the same set of transmission spectra. Fig. 7 shows an example of the measured (blue) and fitted (red) transmission spectrum of the microdisk modulator at revised bias voltage of -1 V, which returns an absorption coefficient of 6.85 dB/mm.

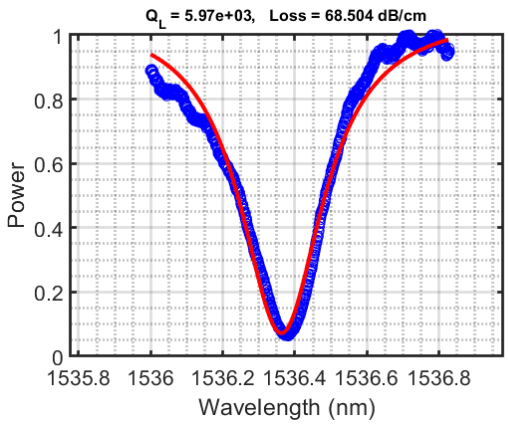

Figure 7. Measured and fitted transmission of the microdisk, showing the absorption coefficient and quality factor of the microdisk under the rever biased voltage at -1 V.

C. Electrical response (S_{11}) of the lumped micro-disk and circuit parameter extraction

Figure 8 shows the three-branch pad model that accurately fits the small-signal RF behavior of the micro-disk modulator:

$$\begin{aligned} Y_{\mathrm{pad}}(\omega) &= j\omega C_{\mathrm{pad}}, \\ Y_{\mathrm{pn}}(\omega) &= \frac{1}{R_{\mathrm{pn}} + \dfrac{1}{j\omega C_{\mathrm{pn}}}}, \\ Y_{\mathrm{sub}}(\omega) &= \frac{1}{R_{\mathrm{sub}} + \dfrac{1}{j\omega C_{\mathrm{box}}}}. \end{aligned} \tag{6}$$

The total shunt admittance is

$$Y_{\mathrm{tot}}(\omega) = Y_{\mathrm{pad}} + Y_{\mathrm{pn}} + Y_{\mathrm{sub}}, \tag{7}$$

the input impedance is $Z_{\mathrm{in}} = 1/Y_{\mathrm{tot}}$, and with a 50 Ω reference

$$S_{11}(\omega) = \frac{Z_{\mathrm{in}}(\omega) - Z_0}{Z_{\mathrm{in}}(\omega) + Z_0}, \qquad Z_0 = 50\ \Omega. \tag{8}$$

A calibrated VNA measures the complex $S_{11}^{\mathrm{meas}}(\omega)$ from 50 MHz to 40.5 GHz using a GS probe. The substrate contact is left floating so that the entire pad model appears between signal and ground. Although all five parameters can be obtained from a single non-linear fit, we follow the procedure of [16, 17]: the pad resistance is fixed to the software simulation value while the remaining parameters are fitted from the measurements. Figure 8 compares the measured and fitted S_{11}; the resulting lumped parameters are summarized in Table I.

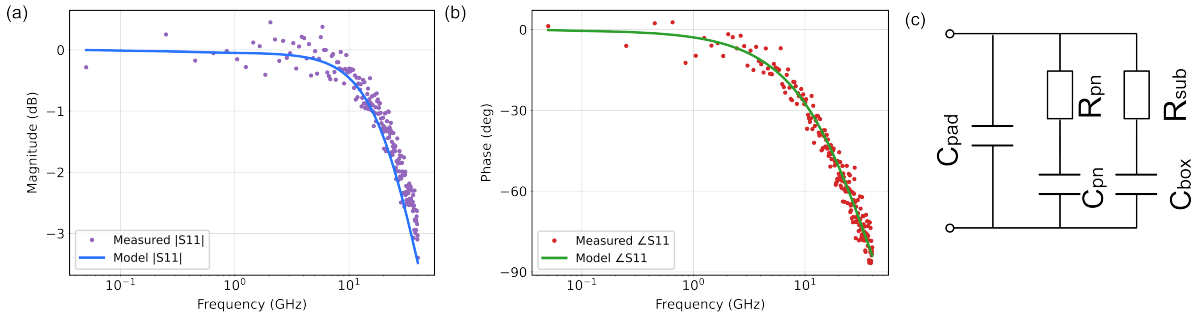

Figure 8. Measured (dots) and fitted (solid line) S_{11} magnitude of the micro-disk.

Table I. Extracted parameters of the microdisk circuit.

C_{pn}	R_{pn}	C_{box}	R_{sub}	C_{pad}
75 fF	23 Ω	34 fF	19 kΩ	3.5 fF

From the above circuit parameter values, the RC determined bandwidth S_{21} was calculated, and the final bandwidth, which is determined by the RC bandwidth and the photon lifetime, was calculated and shown in the main paper. It was noted that the final bandwidth is also determined by the input laser wavelength, a smaller wavelength-resonance difference will decrease the final measured bandwidth.

III. NON-VOLATILE TRIMMING

A. Subsection 1: Laser annealing

The laser annealing was first verified in a SiN microring E/O modulator, the microring is covered with top thick cladding, through the laser annealing, the cladding bonding angle changes, this will increase the cladding compaction, and increase the refractive index. During the annealing process, we capture the leakage intensity from above the microring

directly, The measured leakage intensity versus time is shown in Figure 9, as clearly shown, the microring started with off resonance, through the trimming, the microring gradually becomes to in resonance state, and we can see a clear 'ring shape' leakage, further trimming the microring will make it becomes off resonance again, the leakage intensity gradually increase, when trimmed to the in resonance state, the leakage intensity reach to the highest value, and then gradually decrease with the trimming laser on.

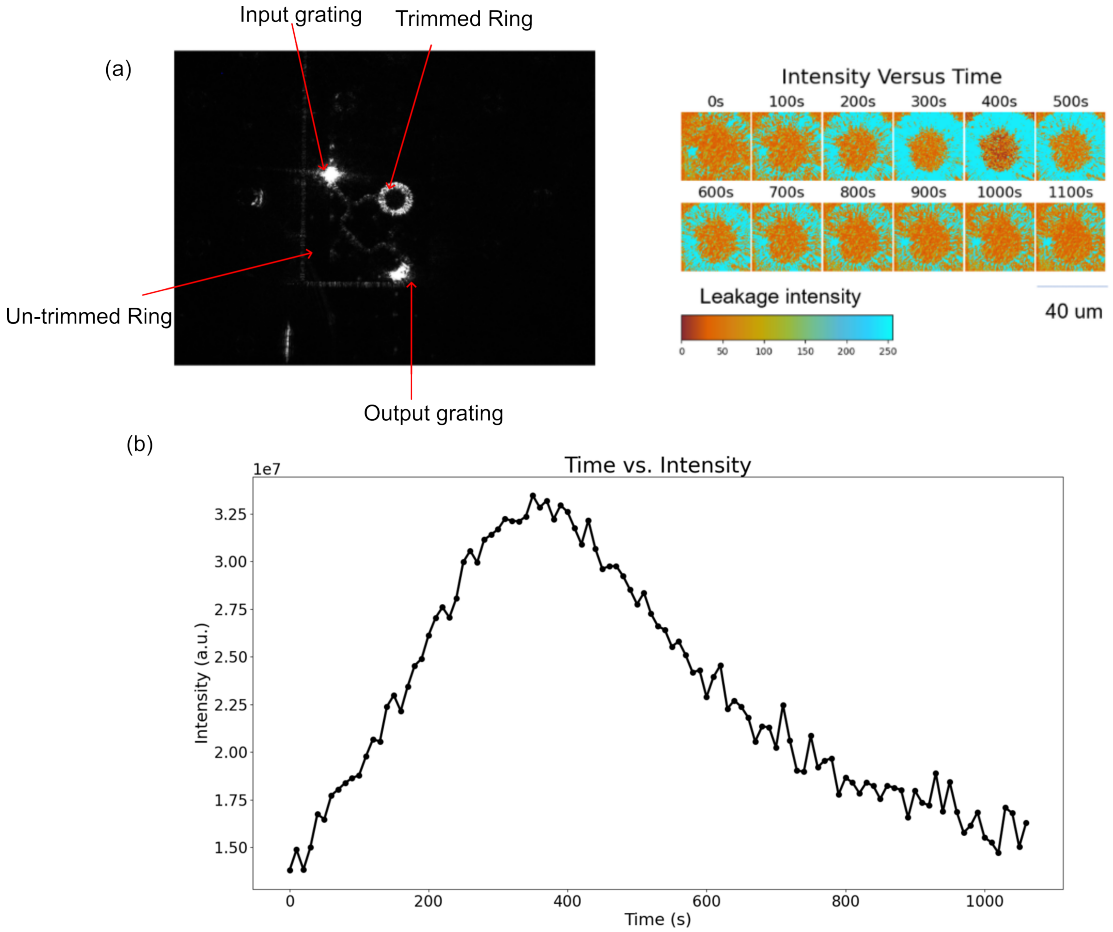

Figure 9. Laser annealing validation in cladding covered SiN E/O modulator.

In the silicon micro-disk the out-of-plane scatter port is masked by the integrated heater, so the resonance shift is monitored at the grating-coupler output. A laser spot with a 1 µm radius ($\approx 3\ \mu m^2$) is used for trimming; its power density is $\sim 1\ mW\,\mu m^{-2}$, well above the SiO_2 densification threshold. Because the optical mode in silicon is much more tightly confined than in SiN, its evanescent overlap with the cladding—and hence the index change produced by compaction—is smaller. Consequently, the cavity resonance shift is between ~ 100 pm to ~ 380 pm, changes among different microdisk due to the SiO_2 quality different of among different devices.

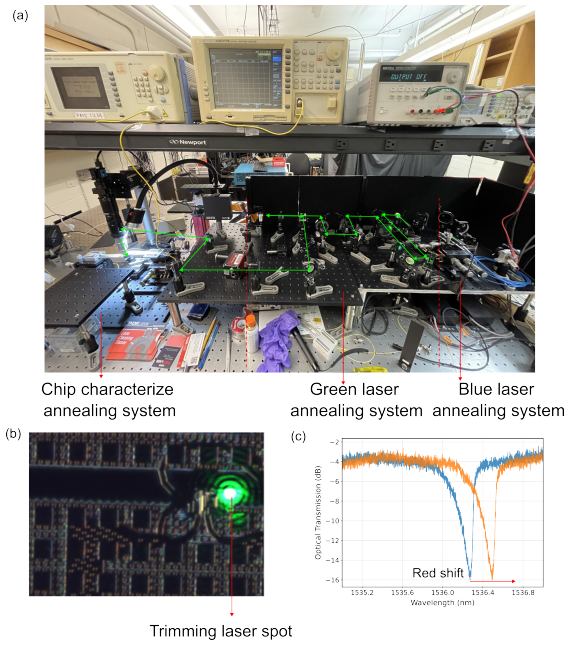

Figure 10. Laser annealing setup and results for the Silicon microdisk E/O modulator, in the experimental setup, we have replaced the galvanometers to spatial light modulator, which support multiple, in parallel trimming, the technique is under development.

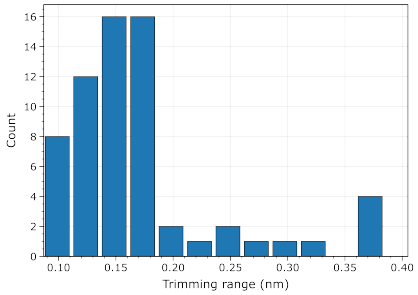

Figure 11. Laser annealing results among different channels.

B. Subsection 2: Reduce the thermal tunning energy consumption

The thermal energy required to tune a resonator scales with the wavelength shift needed to reach the target, $\Delta\lambda = \lambda_{\text{tar}} - \lambda$. Because our trimming method provides only a red shift, devices whose initial resonance exceeds the target ($\lambda_i > \lambda_{\text{tar}}$) are excluded from analysis.

For microdisks with $\lambda_i < \lambda_{\text{tar}}$, we apply a trimming cap C and define the post-trim resonance for device i as

$$\lambda_i'(C) = \min\big(\lambda_i + C,\ \lambda_{\text{tar}}\big). \tag{9}$$

We then compute the ensemble-average resonance over all included devices,

$$\bar{\lambda}(C) = \langle \lambda_i'(C) \rangle, \tag{10}$$

and the residual detuning relative to the target,

$$\varepsilon(C) = \lambda_{\text{tar}} - \bar{\lambda}(C). \tag{11}$$

Since the thermal energy required after trimming is proportional to the remaining wavelength error, the relative energy saving is,

$$S(C) = 1 - \frac{\varepsilon(C)}{\varepsilon(0)}, \tag{12}$$

where $\varepsilon(0)$ is the untrimmed residual detuning computed from the pre-trim ensemble average.

C. Subsection 3: Reduce the design redundancy

We model each of the K WDM channels as provisioned with redundancy r (i.e., up to r rings per channel). Assuming each ring independently lands within the target passband with probability p, the channel success probability is

$$p_{\mathrm{ch}}(p, r) = 1 - (1 - p)^r. \tag{13}$$

Hence, the expected number of usable WDM channels is

$$\mathbb{E}[N] = K\, p_{\mathrm{ch}}(p, r). \tag{14}$$

For a target of at least N_{tgt} usable channels in expectation, the minimal redundancy that satisfies $\mathbb{E}[N] \geq N_{\mathrm{tgt}}$ is

$$r^\star(p; N_{\mathrm{tgt}}, K) \;=\; \left\lceil \frac{\ln\!\big(1 - N_{\mathrm{tgt}}/K\big)}{\ln(1-p)} \right\rceil. \tag{15}$$

Trimming increases the per-ring success probability from $p_{\mathrm{pre}} = 0.0468$ to $p_{\mathrm{post}} = 0.14$. Using (15) with different K number, the required redundancy was calculated, as indicated in Figure 9.

D. Subsection 4: Thermal annealing

Thermal annealing is another widely used post-fabrication trimming technique for resonant silicon photonic devices [42, 43]. By holding the chip at several hundred degree, the SiO_2 cladding densifies and its refractive index increases, permanently shifting the cavity resonance. Furnace exposures of $\sim$ 10–15 min at 400–500°C have been shown to tune passive SiN microrings by more than one free-spectral range with negligible excess loss [43].

Limitation—high temperature. The high process temperature that makes annealing effective for passive structures also limits its applicability to *active* components. Above $\sim$ 300°C aluminium or Titanium heaters can reflow, dopant profiles in p–n junctions smear out, silicide contacts degrade, metal–oxide capacitors, and $p-n$ diode suffer irreversible damage. Consequently furnace annealing is unsuitable for modulators, photodetectors, or devices that incorporate heterogeneous III–V stacks, where even brief high-temperature exposure can compromise speed or reliability. These constraints motivate low-temperature, highly localized alternatives—such as the laser-induced cladding compaction demonstrated in this work—which trim individual resonators without subjecting the rest of the photonic circuit to damaging thermal budgets. We also implement the thermal annealing method in the current chip, we set the thermal heater driving voltage to 8-V, the calculated temperature in the silicon waveguide is about 300°C, turning off the heater driving voltage, we find a 200 pm wavelength red shift. To avoid the potential damage to the modulator, we didn't use this thermal annealing method during the experiment. The issue of the thermal trimmed wavelength shifting is the long time stability, we monitor the resonant wavelength of the thermal trimmed device, and find the resonant wavelength gradually returned to the initial state after 2 weeks, which has been found in other journals [60, 61].

E. Subsection 5: Silicon Oxidation

Oxidizing the silicon core is an attractive post-fabrication technique because the accompanying reduction of the effective refractive index produces a permanent blue-shift of the resonance. In our devices, however, the microrings are buried beneath a thick upper SiO_2 cladding and overlaid by a metal heater wires and contact. We therefore explored a two-step process—wet removal of the cladding followed by thermal oxidation of the exposed waveguide. Before the wet etching we open a window to protect the other part of the device. The window was opened using the lithography and developing. Due to the charging effect, the window was opened using the UV maskless lithography. However, even though the other part of the device is protected using the resist, the HF-based etchlant that stripped the oxide also attacked the heater electrodes, leaving the device electrically open and severely degrading the modulator (Figure 12). Owing to this collateral damage we abandoned the oxide-removal/oxidation route.

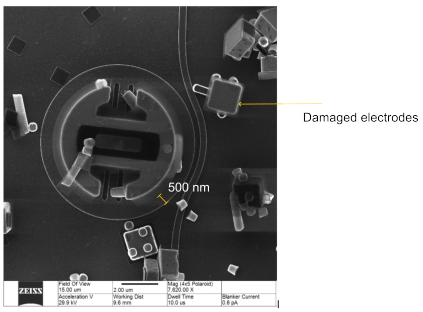

Figure 12. SEM image of the wet etched microdisk, after the resist removing, the electrcode was also damaged.

F. Subsection 4: PCM deposition

Recent years have witnessed significant interest in low-loss phase-change materials (PCMs) such as Sb_2Se_3 (SbSe) and Sb_2S_3 for photonic applications. Their non-volatile nature—maintaining their state without a continuous voltage supply—further enhances their suitability for the trimming application in integrated photonic devices. We also tried to investigate the trimming effect in the current compact microdisk EOIM, however, several facts limits this application:

1. **Metal coverage and limited exposure area.** Unlike other types microring, the microdisk radius is small and most of its surface is already occupied by the p^+/n^+ metal contacts(Figure 13(a,b)). This leaves too little exposed Si (which is 500 nm in our case, as shown in the SEM image) area to open windows, deposit, and pattern a PCM patch. To avoid the damage to other component of the device, like the electrode wires, we need to use lithography to open a window, however, standard AIM-like flows encapsulate the photonic layer under 10 micrometres of SiO_2. Removing (or thinning) this cladding locally introduces topography steps and alignment challenges, as UV maskless exposure has alignment accuracy limitation and while ebeam lithography could provide high alignment accuracy, the top cladding, which is dielectric, prohibited the ebeam alignment due to the strong charging.

2. **No straightforward electrical access.** The vertical junction in the microdisk biases the silicon core, not the PCM layer (Figure 13(c)). Without redesigning the stack into a dedicated metal–PCM–metal (MIM) or metal–PCM–Si (MIS) heater, there is no direct electrical path to Joule-heat (or field-switch) the PCM. Relying solely on indirect substrate heating is inefficient and slow, and the thermal accumulation also damage the microdisk pn junction.

3. **Thermal budget conflict.** Many chalcogenide PCMs (e.g., GST, Sb_2Se_3) require crystallization temperatures >150–$250\,^\circ$C and, in some cases, brief melt–quench cycles near $600\,^\circ$C for re-amorphization. Such temperatures jeopardize doped junctions, metal stacks, and backend dielectrics that are rated for $\lesssim 300$–$350\,^\circ$C.

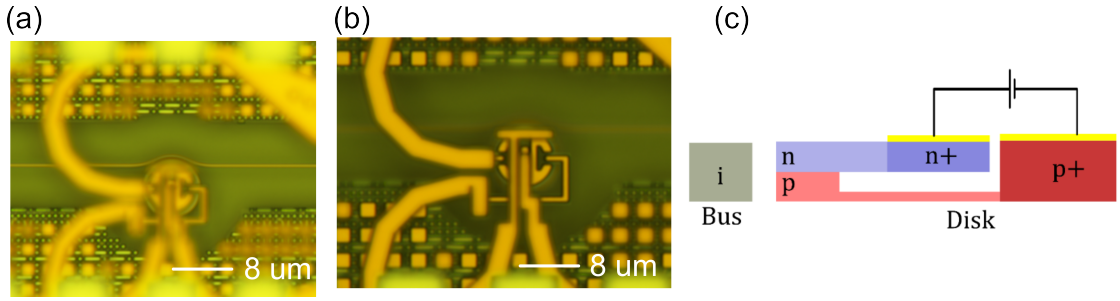

Figure 13. Microscope image and schematic of the microdisk transmitter, where the silicon exposure region is too small and the PCM couldn't be deposited.

In summary, the combination of *(i)* scarce and metal-covered surface area, *(ii)* stringent thermal and contamination limits, *(iii)* lack of a electrical probe path constraints makes conventional PCM trimming schemes poorly suited to this microdisk EOIM architecture.

IV. WIRE BONDED CHIP

Electrical wirebonding was performed by Optelligent, the whole chip has 256 metal wires that need wire bonding, from the wire-bonded chips ,we can clearly see the structure of the chip, which include the input edge coupler, Y-splitter, thermal phase shifter, microdisk modulator, 2D emitter array and 1D emitter array.

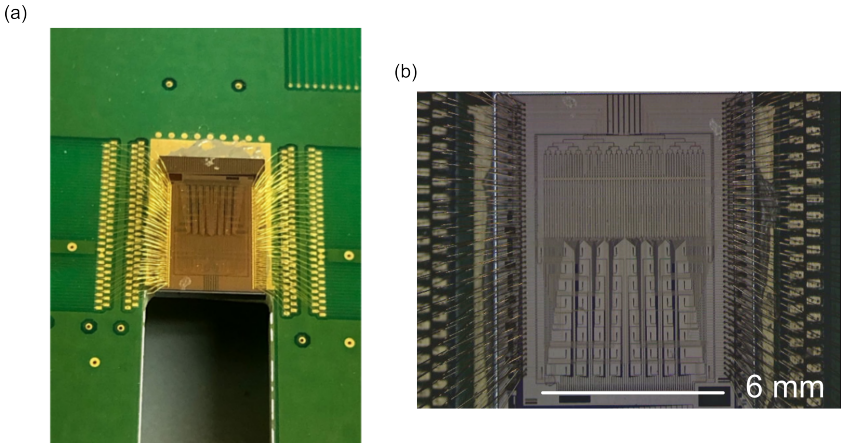

Figure 14. Schematic of the wire-bonded chip.